

Topological semimetal phases in a family of monolayer X_3YZ_6 ($X=\text{Nb,Ta}$, $Y=\text{Si,Ge,Sn}$, $Z=\text{S,Se,Te}$) with abundant nodal lines and nodes

Xing Wang,^{1,2} Wenhui Wan,¹ Yanfeng Ge,¹ and Yong Liu^{1,*}

¹*State Key Laboratory of Metastable Materials Science and Technology & Key Laboratory for Microstructural Material Physics of Hebei Province, School of Science, Yanshan University, Qinhuangdao 066004, China*

²*College of Science, Hebei North University, Zhangjiakou 07500, China*

(Dated: February 17, 2022)

Abstract

The electronic and topological properties of single-layer X_3YZ_6 ($X=\text{Nb,Ta}$, $Y=\text{Si,Ge,Sn}$, $Z=\text{S,Se,Te}$) materials have been studied with the aid of first principles calculations. This kind of materials belong to topological semimetals (TMs) with abundant nodal lines and nodes. Considering their similar properties, we focus on the analysis of Ta_3SnTe_6 and Ta_3SiSe_6 . They have coexisting type-I nodal lines and type-II Dirac points in the absent of spin-orbit coupling (SOC). The nodal lines become Dirac points and original Dirac points disappear in the present of SOC. The three-dimensional (3D) band diagrams reproduce vividly the characteristics of nodes and nodal lines. The appearance of flat bands in (110) edge states further confirm their nontrivial topological properties. We also explore the relationship among different nodal lines (nodes), crystal symmetry and SOC. The type-I nodal lines are protected by crystal symmetry in the absent of SOC. When crystal symmetry is broken, the band structure splits further in the present of SOC. The single-layer X_3YZ_6 materials can be used as candidates for two-dimensional (2D) TMs and provide a platform for further study of interesting physical phenomena.

PACS numbers: 61.46.-w, 61.50.Ah, 73.20.At

I. INTRODUCTION

With the development of topological materials, topological semimetals (TSMs) have become one of the hottest topics in condensed matter physics¹⁻¹⁶, originating from the character of symmetrically or topologically protected band degeneracy near Fermi energy and potential applications. Based on the band crossing points near the Fermi surface, TSMs can be divided into Dirac semimetals (DSMs)³⁻⁵, Weyl semimetals (WSMs)^{6,7}, nodal line semimetals (NLSMs)⁸⁻¹⁰ and multiple degenerate points semimetals^{12,13,15,16}. DSMs have fourfold degenerate band touching points with Dirac cones surface states. WSMs possess twofold degenerate band crosspoint with Fermi-arc surface states. NLSMs are the special cases of DSMs and WSMs with continuously distributed band intersections and drumhead surface states, forming closed ring, nodal links, nodal knots or nodal chains¹¹. Na_3Bi , Cd_3As_2 ^{17,18} and TaAs family^{7,19,20} are the earlier experimentally discovered DSMs or WSMs materials. In addition, NLSMs have also been verified by experimental work^{21,22}, which can host many unusual behavior, such as ultrahigh mobility²³, possible high temperature superconductivity²⁴ and the abnormal optical response²⁵. Although more and more materials are theoretically predicted to be TSMs, the number of TSMs verified by experiment is very small, especially the two-dimensional (2D) NLSMs, whose experimental observation conditions are more demanding. Therefore, it is urgent to propose the TSMs candidate materials for experimental implementation.

Recently, Nb_3GeTe_6 and Nb_3SiTe_6 have attracted a great deal of attention because of their nontrivial topological properties²⁶⁻³². They belong to van der Waals (vdW) materials with two-layer ternary telluride compounds, so the single-layer materials may obtain easily by using mechanical exfoliation method³³. In fact, the bulk single crystals and thin sheets have been synthesized successfully in the laboratory^{30,34}. The bulk Nb_3GeTe_6 and Nb_3SiTe_6 are hourglass semimetals and their nontrivial topological states are guaranteed by nonsymmorphic symmetry^{26,30,32}. Their monolayer materials are NLSMs in the absence of spin-orbit coupling (SOC) and become DSMs in the presence of SOC^{26,32}. Thus far, there are few researches on the monolayer structures of same family or only focused these two materials. On the other hand, the analysis of single-layer topological states is not comprehensive, for example, few literatures can see the description of edge states. Starting from the same family elements, we do more comprehensive researches of these single-layer system and find some interesting results.

In this work, we study systematically the electronic properties of single-layer X_3YZ_6 materials by using first principles calculations. They are all TSMs with rich nodes and nodal lines. X_3YZ_6 family have similar properties close to Ta_3SiSe_6 except Ta_3SnTe_6 , so we take these two materials as examples. The ab initio molecular dynamics (MD) simulations and the phonon calculations suggest they are all thermally and dynamically stable. Without considering SOC, they have coexisting type-I nodal lines and type-II Dirac points. With considering SOC, the nodal lines transform to Dirac points and original Dirac points disappear. The local gap, Fermi surface, Fermi velocity, three-dimensional (3D) band structures and edge states further confirm their nontrivial topological properties. Finally, we prove the nodal line and some nodes are protected by crystal symmetry in the absence of SOC. These results may provide platforms to explore novel physical phenomena and topological states.

II. COMPUTATIONAL DETAILS

The electronic properties of X_3YZ_6 is studied by using the Vienna ab initio Simulation Package (VASP)^{35,36}. The generalized gradient approximation (GGA)³⁷ of Perdew-Burke-Ernzerhof (PBE)³⁸ is treated as the exchange correlation interaction. The monolayer materials extend along the x-y plane, vacuum slab above 15 Å along z-direction is applied to exclude interactions between neighboring images. The Brillouin zone (BZ) is sampled using $10 \times 6 \times 1$ Γ -centered Monkhorst-Pack grid³⁹, the plane-wave cutoff energy is set to 500 eV with the energy precision of 10^{-5} eV. The atomic coordinates are relaxed until the maximum force on each atom is smaller than 0.01 eV/Å. The hybrid functional HSE06⁴⁰ is used to check the results and the resulting band gaps are very similar. The tight binding matrix elements are calculated by projecting the Bloch states onto maximally localized Wannier functions (MLWFs)^{41,42} using the VASPWANNIER90 interface. The X-d, Y-p and Z-p orbitals are used to build the MLWFs by using the Wannier90 code^{41,42}. Topological properties are analysed by using the iterative Green's function method as carried out in the WannierTools package⁴³. The phonon spectra are calculated using density functional perturbation theory (DFPT) PHONOPY code interfaced with VASP⁴⁴.

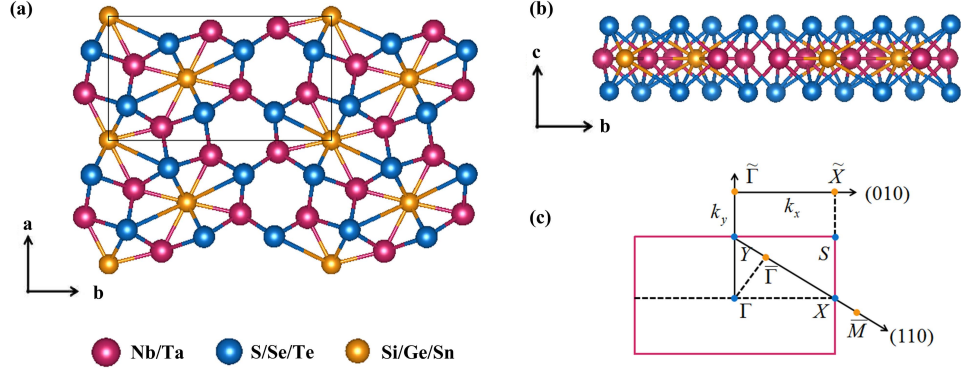


FIG. 1. (Color online) The top view (a) and side view (b) of relaxed single-layer X_3YZ_6 . The primitive cell is shown in black rectangle. (c) 2D and projected edge first BZ with high symmetry points.

III. RESULTS AND DISCUSSION

The X_3YZ_6 ($X=\text{Nb,Ta}$, $Y=\text{Si,Ge,Sn}$, $Z=\text{S,Se,Te}$) monolayer has the orthorhombic structure with $\text{Pmc}21$ (D_{2v}^2) space group shown in Fig. 1 (a, b). The optimized lattice constants of X_3YZ_6 are nearly same to the reference values²⁶ as shown in Table I. While fixed X atoms, the lattice constants have increase trend with increasing atomic radius. While fixed Y and Z atoms, the lattice constants of Nb_3YZ_6 are slightly bigger than Ta_3YZ_6 , which are similar to the $X_3\text{SiTe}_6$ 's²⁶. Monolayer crystals have nonsymmorphic symmetries with a mirror operation M_z ($(x,y,z) \rightarrow (x,y,-z)$) and a glide mirror \tilde{M}_y ($(x,y,z) \rightarrow (x+\frac{1}{2}, -y, z)$). These symmetries provide protection for the topological NLs and Dirac points, we will discuss this latter.

To estimate the feasibility of preparing these monolayers, the cleavage energies are calculated as shown in Table I. The calculated cleavage energy for X_3YZ_6 is between 0.44 and 0.63 J/m², a little bigger than graphene (0.37 J/m²)⁴⁵ and much smaller than CaN_2 (1.14 J/m²)⁴⁶. The graphene have exfoliated successfully in experiment, monolayer X_3YZ_6 may expected to obtain in the same way. Moreover, we examine thermal stability of X_3YZ_6 by performing ab initio MD simulations. The average of the total potential energy stays the same after heating at 300 K for 10ps, see Fig. 2 (a) and supplementary material (SM) Fig. S1. These results indicate clearly the materials remain thermal dynamically stable at room temperature. We also present the Ta_3SnTe_6 monolayer at 1000K and find the structure can still be maintained, so this monolayer has very high thermal stability and may be used to build nanoelectronic devices. The phonon spectra of Ta_3SnTe_6 and Ta_3SiSe_6 are plotted in Fig. 2 (b) and Fig. 6 (a). The absence of imaginary mode in their spectra

indicates dynamical stability. The single-layer X_3YZ_6 have very similar properties, so we mainly discuss Ta_3SnTe_6 and Ta_3SiSe_6 as examples.

The electron localization function (ELF) are usually used to describe and visualize chemical bonds in solids⁴⁷. The ELF represents the probability of finding a pair of electrons at a given position. We have plotted the ELF with an isosurface of 0.78 in Fig. 2 (c). The ELF value is around 0.78 near Sn atoms and Te atoms, which means that electrons are more localized towards Sn and Te atoms. This type of electron localization indicates the ionic type of bonding between Ta and Sn (Te) atoms. To qualitatively analyze the charge transfer of Ta-Te (or Ta-Sn) bond, difference charge density map is plotted in Fig. 2 (d), the yellow/gray region represents charge accumulation/depletion, respectively. The difference pattern indicates the major charge transfer is from Ta atom to Te (or Sn) atom, which is consistent with the characteristics of an ionic bond. The similar results for Ta_3SiSe_6 and Ta_3SiS_6 are presented in Fig. S2.

TABLE I. The lattice constants a , b and cleavage energy E_c of single-layer X_3YZ_6 .

Structure	$a(\text{\AA})$	$b(\text{\AA})$	$E_c(\text{J/m}^2)$	Structure	$a(\text{\AA})$	$b(\text{\AA})$	$E_c(\text{J/m}^2)$
Ta_3SiS_6	5.825	10.851	0.53	Nb_3SiS_6	5.835	10.961	0.46
Ta_3SiSe_6	6.050	11.105	0.44	Nb_3SiSe_6	6.069	11.210	0.44
Ta_3SiTe_6	6.402	11.559	0.44	Nb_3SiTe_6	6.410	11.634	0.63
Ta_3GeTe_6	6.522	11.637	0.49	Nb_3GeTe_6	6.536	11.706	0.50
Ta_3SnTe_6	6.734	11.806	0.42	Nb_3SnTe_6	6.745	11.880	0.50

Having discussed the stability and chemical bonds of the single-layer materials, then the electronic properties are investigated. Here, we have calculated the band structures and projected density of states (PDOS). In the absence of SOC, the Ta_3SnTe_6 displays a semimetal, the valence and conduction bands meet in the vicinity of the Fermi level and show a nodal line L_1 , as plotted in Fig. 3 (a). The energy of the nodal line L_1 varies with 2meV (flat) and it is not coexisting with other trivial bands (clean), making it an ideal NLSMs candidate material⁴⁸. What's more, there is a small band gap of 11 meV at high symmetry points Y labelled D_2 . The red line and point in the picture of the local gap near the Fermi level confirm the existence of L_1 and D_2 , shown in Fig. 4 (a). Nodes and nodal lines are not confined to Fermi energy, but exist in a certain range near Fermi energy, which is a universal phenomenon of topological semimetals^{49,50}. Additional band crossing are observed below the Fermi level in energy range of 0.5 eV, labelled two Dirac

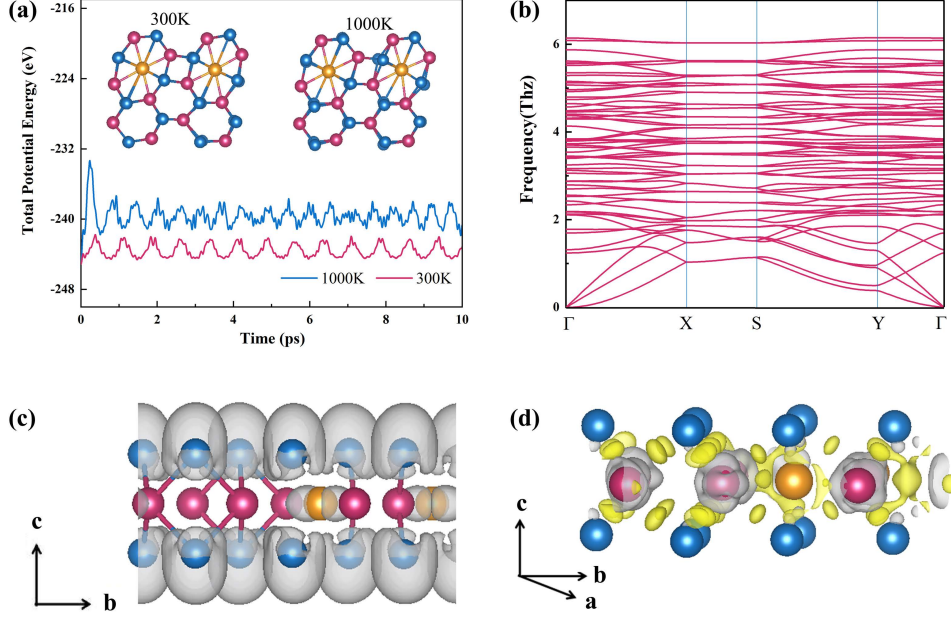


FIG. 2. (Color online) MD simulations (a), phonon spectra (b), ELF (c) and difference charge density (d) of single-layer Ta₃SnTe₆. (a) Snapshots of atomic configurations at the end of MD simulations and total potential energy fluctuations observed at 300K and 1000K, respectively. (c) Isosurface corresponding to ELF value of 0.78. (d) The yellow (gray) isosurface plots correspond to the charge density accumulation (depletion). Isosurface corresponding to difference charge density of $\pm 0.01 \text{ eV/\AA}^3$.

points D₁, D₃ and a nodal line L₂^{49–51}. The obtained Fermi surfaces on the (001) cleaved surface are plotted in Fig. 4 (b), which is consistent with the previous analysis. In the middle, there are two long wavy lines around nodal line L₁ and unsealed oval chain structure surrounding the D₂. The band structures of the Ta₃SiSe₆ indicate it is also a semimetal in Fig. 3 (c), the nodal lines and nodes are similar to the case of Ta₃SnTe₆. The middle red line show the existing of nodal line L₁₁ in Fig. 6 (b), but red point disappears because the band gap at point Y is larger, which leads to closed ellipse Fermi surface structure around it in Fig. 6 (c). The band structure diagrams of the remaining structures of X₃YZ₆ are shown in the Fig. S3, their electronic properties are more closer to case of Ta₃SiSe₆. To illustrate the unique electronic property, we have plotted the PDOS in Fig. 3 (a, c) right panel, which agree well with the band structure distribution. The PDOS clearly show Ta₃SiSe₆ and Ta₃SnTe₆ are metallic. The low-energy states around Fermi level are mainly from the Ta d orbitals, the contribution of Si (or Sn) and Se (or Te) p orbitals are very small.

To reveal the energy dispersion of the nodes and nodal lines, the 3D band structures of Ta₃SnTe₆

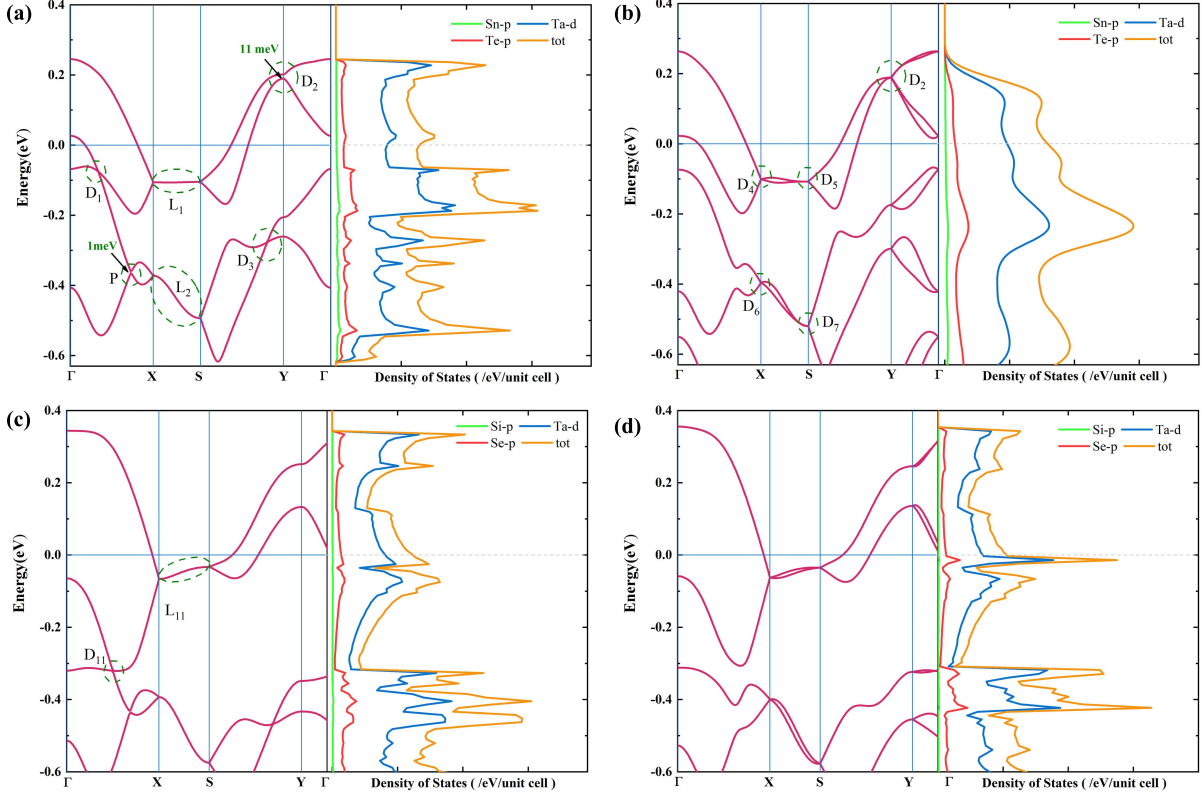


FIG. 3. (Color online) Band structures and projected density of states (PDOS) of single-layer Ta₃SnTe₆ (a, b) and Ta₃SiSe₆ (c, d), respectively. (a, c) without considering the SOC. (b, d) with considering the SOC. The Fermi levels are set to zero.

and Ta₃SiSe₆ are plotted in Fig. 5 (a, c, d) and Fig. 6 (d), respectively. The valence band maximum (VBM) and conduction band minimum (CBM) meet in the vicinity of Fermi level with opposite slopes, which shows type-I^{52,53} nodal lines L₁ and L₁₁. The two bands form nodal line L₂ with opposite slopes, so L₂ is also a type-I nodal line. Although they are all type-I nodal lines, the shapes of the nodal lines are different. They are straight (L₁), parabolic (L₂) and curve (L₁₁), respectively. The D₁, D₃ and D₁₁ are type-II Dirac points, because the two bands are tilted in the same slope sign. The Berry phases around nodal line L₁ and Dirac cone D₁ are π , further supporting the existence of the non-zero Berry phase and the existence of Dirac particles in Ta₃SnTe₆. The nodes and nodal lines near the Fermi surface has extremely high mobility, the Fermi velocity of D₁ is anisotropic and about 2.1×10^5 m/s in (010) surface, compared to HgTe quantum well (5.5×10^5 m/s)⁵⁴.

The edge states are another manifestation of the nontrivial topological properties. The edge

states of (010) and (110) surface are showing in Fig. 4 (c, d) for Ta_3SnTe_6 . According to the energy range of band structure in Fig. 3 (a), the corresponding positions of Dirac points and nodal line are found in the edge states. Another interesting feature of NLSMs is the appearance of flat band in the edge states⁵⁵. Sure enough, we find a flat band labelled L'_1 with its band width being about 14 meV on the (110) surface edge state. Since the edges are electrically neutral, flat bands may be half-filled, providing an interesting platform for strongly correlated physics⁵⁵. The edge states of Ta_3SiSe_6 are similar to the Ta_3SnTe_6 's, we also find the position of nodal line L_{11} and node D_{11} in the edge state, shown in Fig. 6 (e, f). The flat bands confirm the topological nontriviality of Ta_3SnTe_6 and Ta_3SiSe_6 .

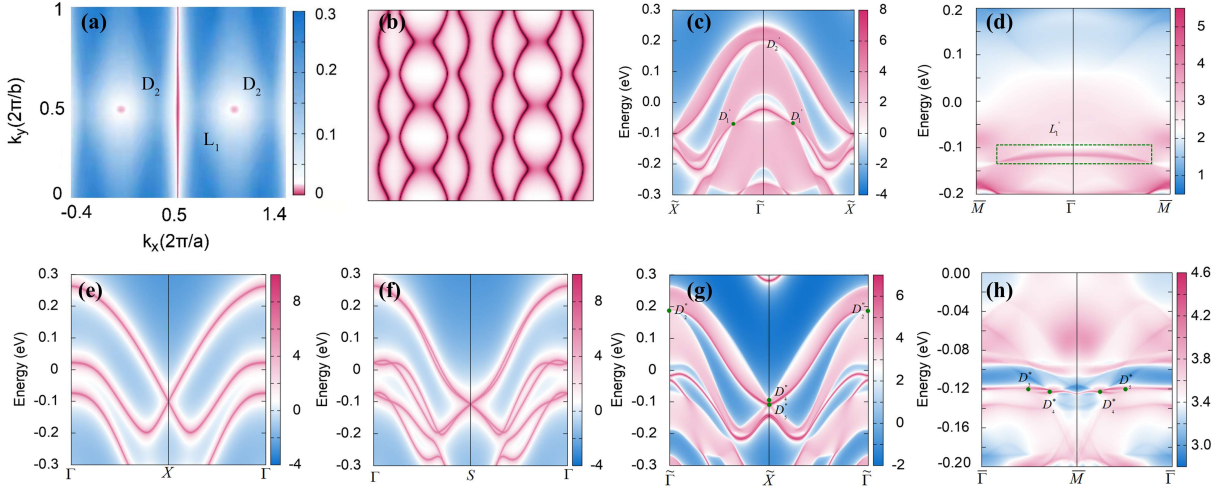


FIG. 4. (Color online) The band gap (a), Fermi surface (b), edge state(c, d, g, h), the zoom-in of the band structure (e, f) for single-layer Ta_3SnTe_6 . (a) The local gap near the Fermi level. (b) The calculated Fermi surface on the $k_z=0$. The edge states on the (c, g) (010) and (d, h) (110) surface, (c, d) without and (g, h) with considering SOC, respectively. The zoom-in of the band structure around the X point (e) and S point (f) with considering SOC, respectively. The Fermi level is set to zero.

Then we discuss the stability of Dirac points and nodal lines under different cases. In the present of SOC, the X_3YZ_6 materials still display semimetal phases, the valence and conduction bands meet in the vicinity of the Fermi level as plotted in Fig. 3 (b, d) and Fig. S3. For Ta_3SnTe_6 , the nodal line L_1 is gapped with a small band gap about 14 meV and form two Dirac points D_4 and D_5 . The case of L_2 is similar to L_1 , the nodal line becomes two Dirac points D_6 and D_7 . The Fermi velocities are about 2.3×10^4 m/s for D_4 and 2.1×10^3 m/s for D_5 in X-S direction, which

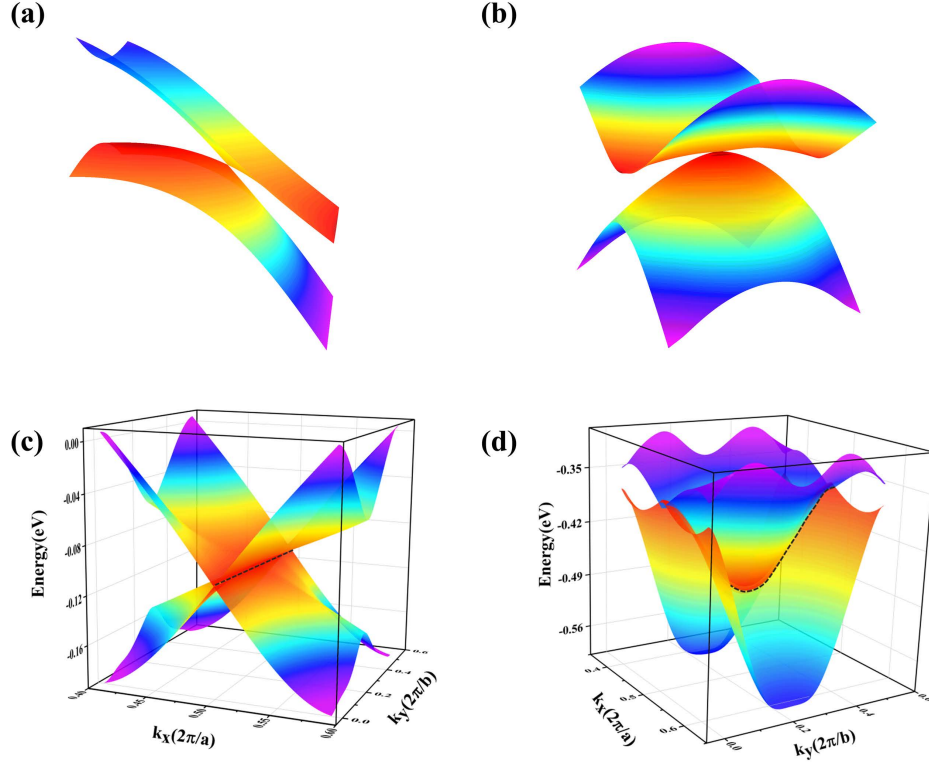


FIG. 5. (Color online) 3D band structures for single-layer Ta_3SnTe_6 . 3D band structures near the Dirac points D_1 (a) and D_2 (b), nodal lines L_1 (c) and L_2 (d), respectively. Nodal lines are denoted by black dotted lines. The different colors indicate the energy values deviating from the Dirac point or nodal line. (a, c, d) without and (b) with considering SOC, respectively. The Fermi level is set to zero.

are close to case in Ta_3SiTe_6 ²⁶. The band intersection P disappears, the band gap of D_2 becomes small and forms a Dirac point. The 3D band structure around D_2 are plotted in Fig. 5 (b), the anisotropic Dirac cone can be clearly seen. The Fermi velocity of D_2 is about 8.8×10^3 m/s in (010) surface. The zoom-in of the band structure around the X point and S point are plotted in Fig. 4 (e, f), the Dirac points become more obvious. The calculated edge states of the (010) and (110) surface are showing in Fig. 4 (g, h), which are another manifestation of the nontrivial topology of the Ta_3SnTe_6 . One can see easily the emergence of topological nontrivial edge states and Dirac points. The changes of nodal lines for Ta_3SiSe_6 is similar to Ta_3SnTe_6 's, but the variation of band gap at the point Y is a little different. For Ta_3SnTe_6 , the band gap at Y point becomes small and forms a Dirac point. But the band gap barely changes for Ta_3SiSe_6 , there is no Dirac point. In fact, the X_3YZ_6 materials except Ta_3SnTe_6 have band gaps at point Y, only Ta_3SnTe_6 have an extra

Dirac point D_2 .

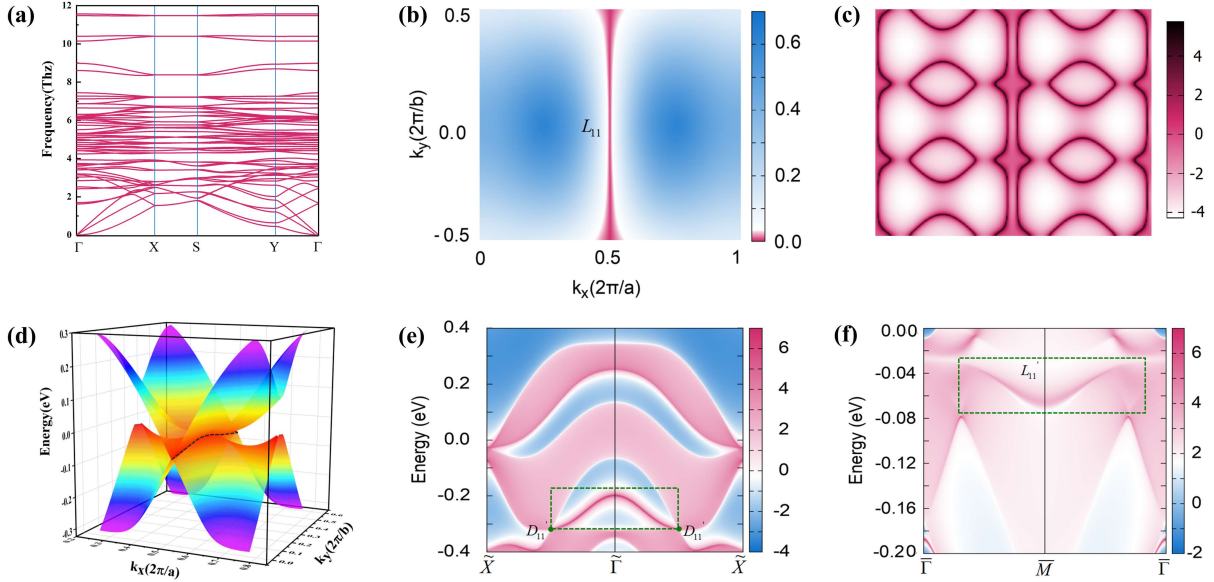


FIG. 6. (Color online) Phonon spectra(a), band gap (b), Fermi surface (c), 3D band structures (d) and edge state(e, f) for single-layer Ta_3SiSe_6 in the absence of the SOC. (b) The local gap near the Fermi level. (c) The calculated Fermi surface on the $k_z=0$. (e) 3D band structures near the nodal lines L_{11} to show its nodal line features. Nodal line is denoted by black dotted line. The different colors indicate the energy values deviating from the nodal line. The edge states on the (e) (010) and (f) (110) surface. The Fermi level is set to zero.

To prove nodes and nodal lines are protected by symmetry, several tests are performed for Ta_3SnTe_6 . First, we artificially shift the positions of the Ta atoms along the c axis to break the mirror symmetry M_z and maintain the \tilde{M}_y in Fig. 7 (a). The node D_1 , nodal lines L_1 and L_2 are all fully gapped, while node D_3 still exists, shown in Fig. 7 (c). These mean D_1 , L_1 and L_2 are protected by M_z symmetry in the absence of SOC. In the present SOC, the band of nodal line splits further to form two double degenerate points in Fig. 7 (e). Second, we shift the positions of the Ta atoms along the a axis to break the mirror symmetry \tilde{M}_y and maintain the M_z symmetry in Fig. 7 (b). The nodes D_1 , D_3 , nodal lines L_1 and L_2 are all fully gapped in the absence of SOC, plotted in Fig. 7 (d), which means D_1 , L_1 and L_2 are protected by \tilde{M}_y symmetry. While D_3 and D_2 are affected by \tilde{M}_y . With considering SOC, the band splits further shown in Fig. 7 (f). To further clarify the relationship between D_2 (or D_3) and symmetry, we perform a third test. We use 10% uniaxial tensile strain along the a axis and b axis direction for single-layer Ta_3SnTe_6 , but the

crystal symmetry stays the same. The band structures are plotted in Fig. 7 (g) (h), we find the gaps of D_1 , L_1 and L_2 are not change, but the gap of D_2 is changed and node D_3 disappears under strain along the a axis, or the gap of D_2 becomes zero and position of D_3 has changed under strain along the b axis. These results show D_1 , L_1 and L_2 are protected by M_z and \tilde{M}_y symmetry, D_2 and D_3 are affected by these two symmetry.

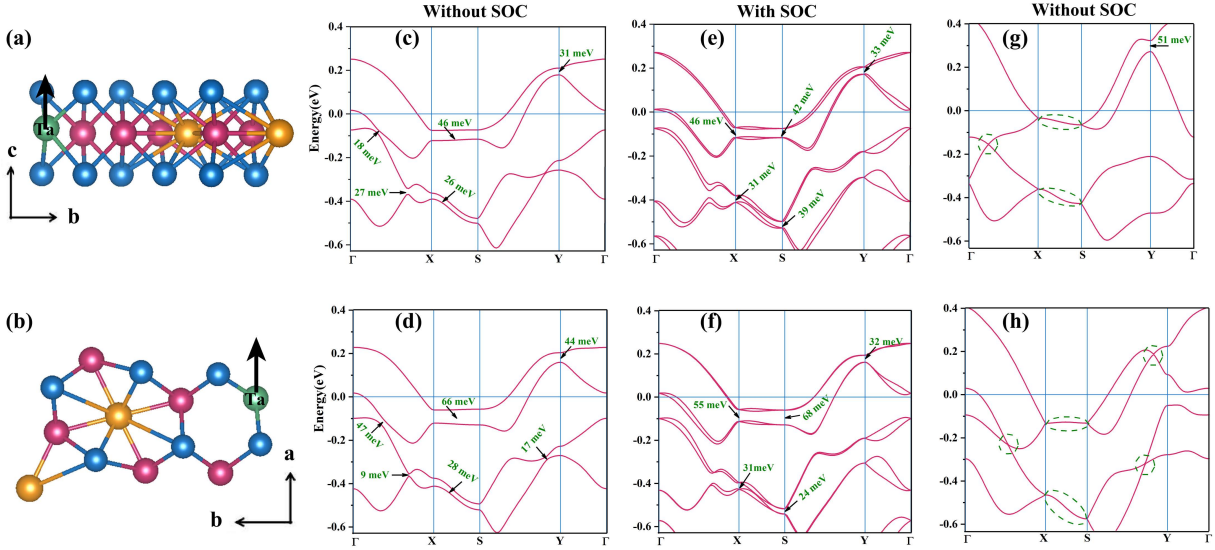


FIG. 7. (Color online) Side view (a) and top view (b) of the crystal structure for single-layer Ta_3SnTe_6 . Black arrows indicate the shift (0.01 \AA) of the Ta atoms along the c axis and a axis, respectively. The band structures (c, d) without and (e, f) with considering SOC after moving, (c, e) and (d, f) for the configuration in (a) and (b), respectively. The band structures under 10% uniaxial tensile strain along the a axis [(g)] and b axis [(h)] direction, respectively. The Fermi level is set to zero.

To test the effect of electron correlation on band structure, we perform GGA + U calculations with considering hubbard U correction of transition metal elements. Compared with GGA, there is little change in the results of single-layer Ta_3SnTe_6 and Ta_3SiSe_6 , shown in Fig. S4 and S5. In addition, we use the hybrid functional HSE06 to check the electronic structure, similar nodes and nodal lines are found for single-layer Ta_3SnTe_6 and Ta_3SiSe_6 without considering the SOC in Fig. S6. We also have analyzed the electronic structure of the two-layer Ta_3SnTe_6 and found the nodes and nodal lines will still exist, as shown in Fig. S7.

IV. CONCLUSION

In summary, we find the monolayer X_3YZ_6 have similar properties and they are all TSMs materials based on the first principles calculations. The MD simulations indicate they are all thermal-dynamically stable. Taken Ta_3SnTe_6 and Ta_3SiSe_6 as examples, they have coexisting type-I nodal lines and type-II Dirac points in the absent of SOC. With the presence of SOC, the nodal lines become Dirac points and original Dirac points disappear. The characteristics of nodal lines and nodes can be clearly seen by using 3D band diagrams. Their nontrivial topological properties are confirmed by (010) and (110) surface edge states. The relationship among different nodal lines (nodes), crystal symmetry and SOC has been discussed. D_1 , L_1 and L_2 are protected by M_z and \tilde{M}_y symmetry, D_2 and D_3 are affected by these two symmetry for Ta_3SnTe_6 . The SOC cause the band to split further. X_3YZ_6 materials can be ideal candidates for the nodal line and node TSMs. These results can be used as a supplement to the research content of Ta_3SiTe_6 and provide theoretical basis for subsequent experimental research.

ACKNOWLEDGMENTS

This work was supported by National Natural Science Foundation of China (No. 11904312 and 11904313), the Project of Department of Education of Hebei Province, China(No. BJ2020015), and the Natural Science Foundation of Hebei Province (No. A2019203507 and A2020203027). The authors thank the High Performance Computing Center of Yanshan University.

* yongliu@ysu.edu.cn, or ycliu@ysu.edu.cn

- ¹ K. S. Novoselov, A. K. Geim, S. V. Morozov, D. Jiang, Y. Zhang, S. V. Dubonos, I. V. Grigorieva, and A. A. Firsov, *Science* **306**, 666(2004).
- ² Y. Zhang, Y. W. Tan, H. L. Stormer, and P. Kim, *Nature* **438**, 201(2005).
- ³ Z. J. Wang, Y. Sun, X. Q. Chen, F. Cesare, and X. Gang, *Phys. Rev. B* **85**, 195320(2012).
- ⁴ Z. Wang, H. Weng, Q. Wu, X. Dai, and Z. Fang, *Phys. Rev. B* **88**, 125427(2013).
- ⁵ S. M. Young, S. Zaheer, J. C. Y. Teo, C. L. Kane, E. J. Mele, and A. M. Rappe, *Phys. Rev. Lett.* **108**, 140405(2012).
- ⁶ H. M. Weng, C. Fang, Z. Fang, B. A. Bernevig, and X. Dai, *Phys. Rev. X* **5**, 011029 (2015).

- ⁷ B. Q. Lv, H. M. Weng, B. B. Fu, X. P. Wang, H. Miao, J. Ma, P. Richard, X. C. Huang, and L. X. Zhao, Phys. Rev. X **5**, 031013(2015).
- ⁸ A. A. Burkov, M. D. Hook, and L. Balents, Phys. Rev. B **84**, 4319(2011).
- ⁹ H. M. Weng, Y. Y. Liang, Q. Xu, R. Yu, Z. Fang, and X. Dai, Phys. Rev. B **92**, 045108(2015).
- ¹⁰ K. Mullen, B. Uchoa, and D. T. Glatzhofer, Phys. Rev. Lett. **115**, 026403(2015).
- ¹¹ C. J. Yi, B. Q. Lv, Q. S. Wu, B. B. Fu, X. Gao, and M. Yang, Phys. Rev. B **97**, 201107(2018).
- ¹² B. Bradlyn, J. Cano, Z. Wang, M. G. Vergniory, C. Felser, and R. J. Cava, Science **353**, 6299(2016).
- ¹³ Z. Zhu, G. W. Winkler, Q. S. Wu, J. Li, and A. A. Soluyanov, Phys. Rev. X **6**, 031003(2016).
- ¹⁴ H. M. Weng, C. Fang, Z. Fang, and X. Dai, Phys. Rev. B **94**, 165201(2016).
- ¹⁵ T. T. Heikkil and G. E. Volovik, New J. Phys. **17**, 093019(2015).
- ¹⁶ B. Q. Lv, Z. L. Feng, Q. N. Xu, X. Gao, and J. Z. Ma, Nature **546**, 627(2017).
- ¹⁷ Z. K. Liu, B. Zhou, Y. Zhang, Z. J. Wang, H. M. Weng, D. Prabhakaran, S. K. Mo, Z. X. Shen, Z. Fang, and X. Dai, Science **343**, 864(2014).
- ¹⁸ Z. K. Liu, J. Jiang, B. Zhou, Z. J. Wang, Y. Zhang, and H. M. Weng, Nat. Matter. **13**, 677(2014).
- ¹⁹ B. Lv, N. Xu, H. M. Weng, and J. Z. Ma, Nat. Phys. **11**, 724(2015).
- ²⁰ X. Huang, L. Zhao, Y. Long, P. Wang, D. Chen, Z. Yang, H. Liang, M. Xue, H. Weng, and Z. Fang, Phys. Rev. X **5**, 031023(2015).
- ²¹ G. Bian, T. R. Chang, R. Sankar, S. Y. Xu, H. Zheng, T. Neupert, C. K. Chiu, and S. M. Huang, Nat. Commun. **7**, 10556(2016).
- ²² I. Belopolski, K. Manna, D. S. Sanchez, G. Q. Chang, and M. Z. Hasan, Science **365**, 1278(2019).
- ²³ J. Hu, Z. J. Tang, J. Y. Liu, Y. L. Zhu, J. Wei, and Z. Q. Mao, Phys. Rev. B **96**, 045127(2017).
- ²⁴ S. Y. Guan, P. J. Chen, M. W. Chu, R. Sankar, F. Chou, H. T. Jeng, C. S. Chang, and T. M. Chuang, Sci. Adv. **2**, e1600894(2016).
- ²⁵ S. Ahn, E. J. Mele, and H. Min, Phys. Rev. Lett. **119**, 147402(2017).
- ²⁶ S. Li, Y. Liu, S. S. Wang, Z. M. Yu, S. Guan, X. L. Sheng, Y. G. Yao, and S. Y. Yang, Phys. Rev. B **97**, 045131(2018).
- ²⁷ T. Sato, Z. W. Wang, K. Nakayama, S. Souma, D. Takane, Y. Nakata, H. Iwasawa, C. Cacho, T. Kim, T. Takahashi, and Y. Ando, Phys. Rev. B **98**, 121111 (2018).
- ²⁸ L. L. An, H. Zhang, J. Hu, X. D. Zhu, W. S. Gao, J. L. Zhang, C. Y. Xi, W. Ning, Z. Q. Mao, and M. L. Tian, Phys. Rev. B **97**, 235133(2018).

- ²⁹ M. Naveed, F. C. Fei, H. J. Bu, X. Y. Bo, S. A. Shah, B. Chen, Y. Zhang, Q. Q. Liu, B. Y. Wei, S. Zhang, J. W. Guo, C. Y. Xi, A. Rahman, Z. M. Zhang, M. H. Zhang, X. G. Wan, and F. Q. Song, *Appl. Phys. Lett.* **116**, 92402(2020).
- ³⁰ Q. Wan, T. Y. Yang, S. Li, M. Yang, Z. Zhu, C. L. Wu, C. Peng, S. K. Mo, W. Wu, Z. H. Chen, Y. B. Huang, L. L. Lev, V. N. Strocov, J. Hu, and Z. Q. Mao, *Phys. Rev. B* **103**, 165107(2021).
- ³¹ S. Roy, R. Singha, A. Ghosh, and P. Mandal, *Phys. Rev. Mater.* **5**, 064203(2021).
- ³² X. T. Wang, G. Q. Ding, S. Khandy, Z. Cheng, G. Zhang, X. L. Wang, and H. Chen, *Nanoscale* **12**, 16910(2020).
- ³³ K. S. Novoselov, D. Jiang, F. Schedin, T. J. Booth, and V. V. Khotkevich, *Proc. Natl. Acad. Sci.* **102**, 10451(2005).
- ³⁴ J. Hu, X. Liu, C. L. Yue, J. Y. Liu, H. W. Zhu, J. B. He, J. Wei, Z. Q. Mao, L. Y. Antipina, Z. I. Popov, P. B. Sorokin, T. J. Liu, P. W. Adams, S. M. A. Radmanesh, L. Spinu, H. Ji, and D. Natelson, *Nat. Phys.* **11**, 471 (2015).
- ³⁵ G. Kresse and J. Furthmuller, *Phys. Rev. B* **54**, 11169(1996).
- ³⁶ G. Kresse and J. Furthmuller, *Comput. Mater. Sci.* **6**, 15(1996).
- ³⁷ J. P. Perdew and J. A. Chevary, *Phys. Rev. B* **46**, 6671(1992).
- ³⁸ J. P. Perdew, K. Burke, and M. Ernzerhof, *Phys. Rev. Lett.* **78**, 3865(1996).
- ³⁹ H. J. Monkhorst and J. D. Pack, *Phys. Rev. B* **13**, 5188(1976).
- ⁴⁰ J. Heyd, G. E. Scuseria, and M. Ernzerhof, *J. Chem. Phys.* **118**, 8207(2006).
- ⁴¹ N. Marzari and D. Vanderbilt, *Phys. Rev. B* **56**, 12847(1997).
- ⁴² S. Ivo, M. Nicola, and V. David, *Phys. Rev. B* **65**, 035109(2001).
- ⁴³ Q. Wu, S. Zhang, and H. F. Song, *Comput. Phys. Commun.* **224**, 405(2018).
- ⁴⁴ S. Baroni, S. D. Gironcoli, A. D. Corso, and P. Giannozzi, *Rev. Mod. Phys.* **73**, 515(2001).
- ⁴⁵ R. Zacharia, H. Ulbricht, and T. Hertel, *Phys. Rev. B* **69**, 155406(2004).
- ⁴⁶ S. Zhao, Z. Li, and J. Yang, *J. Am. Chem. Soc.* **136**, 13313(2014).
- ⁴⁷ A. Savin, R. Nesper, S. Wengert, and T. F. Fassler, *Angew. Chem. Int. Ed. Engl.* **36**, 1808(1997).
- ⁴⁸ R. W. Zhang, X. D. Zhou, Z. Y. Zhang, D. S. Ma, Z. M. Yu, W. X. Feng, and Y. G. Yao, *Nano Lett.* **21**, 8749(2021).
- ⁴⁹ B. S. Wang, H. Gao, Q. Lu, W. H. Xie, Y. F. Ge, Y. H. Zhao, K. C. Zhang, and Y. Liu, *Phys. Rev. B* **98**, 115164(2018).
- ⁵⁰ Y. L. Jiao, F. X. Ma, C. M. Zhang, J. Bell, S. Sanvito, and A. J. Du, *Phys. Rev. Lett.* **119**, 016403(2017).

- ⁵¹ P. Zhou, Z. Ma, and L. Sun, J. Mater. Chem. C **6**, 1206(2018).
- ⁵² S. Li, Z. M. Yu, Y. Liu, S. Guan, S. S. Wang, X. M. Zhang, Y. G. Yao, and S. A. Yang, Phys. Rev. B **96**, 081106(2017).
- ⁵³ X. Zhang, L. Jin, X. Dai, and G. Liu, J. Phys. Chem. Lett. **8**, 4814(2017).
- ⁵⁴ Y. Xu, B. Yan, H. J. Zhang, J. Wang, X. Gang, P. Tang, W. Duan, and S. C. Zhang, Phys. Rev. Lett. **111**, 136804(2013).
- ⁵⁵ B. Yang, X. M. Zhang, and M. W. Zhao, Nanoscale **9**, 8740(2017).